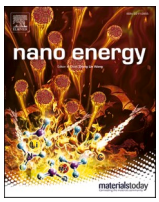
Nano Energy 85 (2021) 105978



Contents lists available at ScienceDirect

Nano Energy

journal homepage: http://www.elsevier.com/locate/nanoen





Morphology-controllable wrinkled hierarchical structure and its application to superhydrophobic triboelectric nanogenerator

Junseong Ahn [a,b], Zhi-Jun Zhao [b], Jungrak Choi [a], Yongrok Jeong [b], Soonhyoung Hwang [b], Jiwoo Ko [a,b], Jimin Gu [a], Sohee Jeon [b], Jaeho Park [a], Mingu Kang [a], Dionisio V. Del Orbe [a], Incheol Cho [a], Hyeokjung Kang [b], Moonjeong Bok [b], Jun-Ho Jeong [b,*], Inkyu Park [a,*]

[a] Department of Mechanical Engineering, Korea Advanced Institute of Science and Technology (KAIST), Daejeon 34141, Republic of Korea
[b] Department of Nano Manufacturing Technology, Korea Institute of Machinery and Materials (KIMM), Daejeon 34103, Republic of Korea

ARTICLE INFO

Keywords:
Hierarchical structure
Wrinkle
Superhydrophobic surface
Triboelectric nanogenerator
Cough sensor

ABSTRACT

Hierarchical structures allow one to improve device performance by exploiting the synergistic effects of micro/nano multiscale components. However, the structural complexity of hierarchical structures places limits on their fabrication and applications. Herein, a novel morphology-controllable wrinkled micro/nano hierarchical structure (WHS) was developed by integrating micropatterns, nanopatterns, and wrinkles on a single substrate to overcome these limitations. Each structure could be individually controlled, which offers unlimited design diversity. The produced WHS was used as a superhydrophobic triboelectric nanogenerator. Compared to a nanogenerator with on a film structure, the WHS-based nanogenerator showed a superior contact angle of 152.5°, which is indicative of high hydrophobicity, and an enhanced (by 608%) triboelectric effect, which was ascribed to the highly rough surface of the WHS. The WHS-based nanogenerator was used to fabricate a self-powered and water-repellent cough detection sensor with an entirely superhydrophobic structure and stable superior sensing performance during repeated water spraying.

1. Introduction

The superior properties of certain artificial and natural materials can be ascribed to their multiscale structures [1]. Micro/nano hierarchical structures are characterized by the synergistic effect between the micro- and nanoscale components, which determines the physicochemical properties of the entire structure. For example, the gecko-foot hierarchical structure exhibits strong adhesion, easy detachment, and reversibility due to an increase in intermolecular forces between this structure and its contact surface [2]. In addition, well-designed hierarchical structures offer elevated surface area and roughness, thus featuring superhydrophobicity and self-cleaning ability [3]. Three-dimensional (3D) hierarchical structures can be effectively used not only to fabricate biomimetic functional surfaces such as those mimicking gecko feet [4] and lotus leaves [5], but also to improve the performance of electronic devices such as chemical sensors [6], fuel cells [7], and energy harvesting devices [8]. Therefore, over the past few decades, much research has been conducted to realize and utilize hierarchical structures.

3D hierarchical structures are commonly constructed by combining micro/nanopatterns and wrinkles [9–11]. These components not only provide high surface area, but can also endow the hierarchical structure with the desired properties. For example, nanopatterns can provide functional characteristics such as hydrophobicity/hydrophilicity [12], structural color [13], and nanoscale surface roughness [14], while micropatterns can be used to tune the mechanical properties such as mechanical strength and elasticity [15]. In addition, wrinkles provide highly dense multiscale curved structures that can exhibit stretchability and highly elevated surface areas [16].

However, despite the excellence of 3D hierarchical structures in various fields and the availability of numerous structural designs that were previously developed, the structural complexity of these structures hinders their fabrication and the synergistic implementation of their characteristics. As micro/nano hierarchical structures comprise two or more structures with different scales, they are difficult to produce using conventional micro/nano fabrication methods such as photolithography and 2D/3D printing. Therefore, novel fabrication methods allowing one to implement diverse hierarchical structures are being intensively

* Corresponding authors.
E-mail addresses: jhjeong@kimm.re.kr (J.-H. Jeong), inkyu@kaist.ac.kr (I. Park).

https://doi.org/10.1016/j.nanoen.2021.105978
Received 21 December 2020; Received in revised form 20 February 2021; Accepted 10 March 2021
Available online 17 March 2021
2211-2855/© 2021 Elsevier Ltd. All rights reserved.

researched.

For example, Kim et al. [17,18] developed a multistep optical patterning method and used it to fabricate a uniform micro/nano hierarchical structure by employing multiple patterned masks with different pattern sizes. Advantageously, this method can be used to design and stack various patterns in the vertical direction, although the use of a rigid substrate precludes the integration of wrinkles. In addition, each step of this method affects the underlayer, as the same substrate is sequentially deformed to create a hierarchical structure. As an alternative, Odom's group [16,19–21] has studied hierarchical structures based on multilayered wrinkles, creating hierarchical structures with wrinkles via the mechanical deformation (e.g., buckling and heating-induced shrinkage) of substrates. This method allows one to control the periodicity and nanostructure orientation of wrinkles as well as to easily fabricate hierarchical structures, thus being useful for preparing large-area superhydrophobic substrates. However, as the process relies on mechanical instability, only wrinkles (and not regular patterns) can be formed, and pattern control beyond orientation is difficult. In addition, much effort has been directed at the fabrication of 3D hierarchical structures by combining the buckling effect with nanoimprinting [22] or photolithography with the buckling method [23]. However, the integration of all three structures into a single substrate remains challenging, as a deformable substrate is required to produce wrinkled structures, while micro- and nanopatterns can be easily fabricated on rigid substrates. In addition, a fabrication method that can provide unlimited design diversity based on the independent control of each structure is required. This will enable all three structures to be optimized independently for a given application.

Herein, we developed a morphology-controllable wrinkled micro/nano hierarchical structure (WHS) by using a novel method combining nanotransfer, molding, and the buckling effect to integrate micropatterns, nanopatterns, and wrinkles on a single substrate. To the best of our knowledge, this integration and controllability has been challenging to accomplish, especially for nanostructures. In our case, multilayered nanopatterns were transferred to increase the shape diversity, whereas previously reported hierarchical structures had single-layer nanopatterns. In addition, micropatterns and wrinkles were independently controlled on the same substrate by utilizing the tendency of wrinkles to concentrate in areas with lower stiffness (e.g., the regions without micropatterning). Therefore, the micropatterns retained their original shape during wrinkle fabrication.

When individual functions are assigned to each structure, the WHS can be used as a functional device with the different hierarchical structures acting synergistically. To demonstrate the performance and practicality of the developed WHS, we used it to construct a superhydrophobic triboelectric nanogenerator (S-TENG), in which multilayered nanopatterns and wrinkles increased the surface roughness and surface area, while the microstructured elastomer enhanced the aspect ratio and uniformity of the surface to maximize the hydrophobicity and triboelectric effect. The S-TENG was designed to have superhydrophobic positive and negative triboelectric substrates, whereas only one electrode is hydrophobic in conventional hydrophobic TENGs. Finally, the S-TENG was attached to a reusable mask to fabricate a self-powered and water-repellent cough detection sensor with enhanced performance and stability.

2. Materials and methods

2.1. Micropatterned elastomer fabrication

A schematic illustration of the fabrication process is shown in Fig. S1. For elastomer microstructuring (Fig. S1-1), SU-8 was patterned on a Si wafer by photolithographically using an SU-8 mold using a stepper (MDA-8000B, Midas System, Korea) and then treated with a self-assembled monolayer (trichloro(1*H*,1*H*,2*H*,2*H*-perfluorooctyl)silane, Sigma-Aldrich, USA) to facilitate the separation of the polymer from the SU-8 mold. Subsequently, a commercial elastomer precursor (Dragon Skin 10 NV, HYUP SHIN, Korea) was poured on the SU-8 mold and cured. The micropatterned elastomer was separated from the SU-8 mold and used as a substrate for the WHS.

2.2. Fabrication of multilayered nanopatterns on polyvinyl alcohol (PVA) film

To produce multilayered nanopatterns on a commercial polyvinyl alcohol (PVA) film (Alibaba, China) (Fig. S1-2), a nanopatterned polymer mold was fabricated using a Si master prepared by KrF lithography. For polymer mold replication, RM-311 resin (Minuta Technology Co., Ltd., Korea; polyurethane) was poured onto the prepared Si master. A transparent polyethylene terephthalate (PET) film was used as a substrate to cover the resin. To facilitate the complete penetration of the resin into the nanopatterns of the Si master, pressure was applied using a hand roller. Then, UV light was used to fully polymerize the resin and thus form the polymer mold by separating it from the Si master. This process could be repeatedly replicated using the Si master, and various nanopatterns could be fabricated using the developed method. The detailed fabrication of the polymer mold from the Si master is described in our previous works [24–28]. Then, a 40-nm Au layer was deposited using an e-beam evaporator (Daeki Hi-Tech Co. Ltd., Korea) and transferred onto the PVA film at a temperature above the PVA glass transition temperature. In this transfer process, the first nanopattern layer was transferred by mechanical interlocking with the rubbery substrate, and subsequent layers were transferred via metallic bonding, as discussed in our previous works. Multilayered nanopatterns could be fabricated on the PVA film by repeating this process.

2.3. Fabrication of wrinkles and integration

For hierarchical structuring on the elastomer (Fig. S1-3), the micropatterned elastomer was treated with (3-aminopropyl)triethoxysilane (APTES; Sigma-Aldrich, USA) and coated with a UV-curable adhesive (NOA 61, Sigma-Aldrich, USA) to facilitate adhesion between the elastomer and Au [25]. Then, the multilayered nanopatterns were attached to the elastomer under pre-strain (Table S1), which was applied using a customized biaxial stage (Fig. S2). The biaxial stage was then immersed into hot water at 90 °C for 2 h to remove PVA, and pre-strain was released to afford the WHS.

2.4. Contact angle measurements

Prior to contact angle measurements (DO4010 contact angle meter, Kruss GmbH, Germany), the substrates were treated with a self-assembled monolayer (trichloro(1*H*,1*H*,2*H*,2*H*-perfluorooctyl)silane; Sigma-Aldrich, USA) to render the inherently hydrophilic Au to a hydrophobic state and to increase the hydrophobicity of perfluoropolyether (PFPE). To measure the contact angle, a 10-μm droplet of DI water was placed on the surface of each sample.

2.5. TENG fabrication

First, for the negative triboelectric substrate, a nanopatterned PFPE was fabricated. The UV-curable PFPE resin was poured onto the Si master mold with nanoscale line patterns, imprinted using a roller, and cured using UV light for 3 min. After detachment of the nanopatterned PFPE film from the master, a 40-nm-thick Au electrode was deposited on this film and connected to a wire using Ag paste. Second, for the positive triboelectric substrate, the wire was also connected to the WHS using Ag paste. The electrode region was covered with an epoxy adhesive to enable shielding from the droplet.

2.6. S-TENG characterization

An electrodynamic shaker (The Modal Shop, USA) was used to vibrate the device at various frequencies. The shaker was controlled using a waveform generator (33210A, Keysight, USA), and the electric signals, including open-circuit voltage, current density, and charge density, were measured using an electrometer (6514, Tektronix, USA) and an oscilloscope (MDO3022, Tektronix, USA). The measurement equipment was connected to a laptop for data logging. In addition, the contact force was measured by a load cell of a tensile tester (Shimadzu, Japan). The detailed measurement setup is shown in Fig. S3.

2.7. Characteristics of S-TENG and its application to cough detection

To verify the sensing performance of the S-TENG, water was sprayed at a specific time during device vibration at an input signal of 4 Hz, and the open-circuit voltage was measured. Subsequently, the positive triboelectric substrate was attached to the outer layer of a commercial reusable mask (Magic V-line mask, Yepdog, Korea), and the negative triboelectric substrate was attached to the exhalation valve of the mask inner layer. The outer layer of the mask was separated from the inner layer by four spacers with a distance of 1.5 cm. An oscilloscope (MDO3022, Tektronix, USA) was used to measure the open-circuit voltage in real time.

3. Results and discussion

3.1. Fabrication of morphology-controllable WHSs

Fig. 1 shows a schematic of WHS fabrication and related scanning electron microscopy (SEM) images. As mentioned above, a combination of nanotransfer, molding, and buckling methods was used. First, multilayered Au nanopatterns on a polyurethane acrylate (PUA) mold, which was fabricated by a nanoimprinting process, were transferred onto a water-soluble PVA film (Fig. 1a). Our previous study showed that nanopatterns can be transferred onto a semicrystalline polymer substrate at its glass transition temperature [29]. In this transfer process, the first layer of nanopatterns is transferred by mechanical interlocking with the rubbery substrate, and subsequent layers are transferred via metallic bonding, which is denoted as nanowelding. This method allows not only the design of various nanopatterns but also the fabrication of 3D multilayered nanostructures. Second, a microhole patterned SU-8 mold was photolithographically fabricated, and a micropillar patterned elastomer was then molded using the SU-8 mold. In this step, arbitrary microsize patterns, instead of microhole patterns, can be utilized depending on the desired application. Finally, pre-strain was applied to the patterned elastomer to afford high-density wrinkle structures. The nanostructured PVA film was then attached to the elastomer using a UV-curable adhesive, and the PVA (except for nanostructures) was removed in hot water (Fig. 1b). In this process, wrinkles are generated by the compressive buckling of the stiff Au and adhesive skin layers on the pre-strained substrate [30]. In addition, even though pre-strain was applied to the entire elastomer, the pillars maintained their original shape and pattern owing to their relatively large thickness and high effective stiffness (Fig. S4), as the pre-strain tends to concentrate in the areas with lower stiffness. Since the wrinkles were formed only between the pillars, the wrinkles and micropatterns were controlled independently. In addition, the use of an adhesive to attach the nanopatterns to the micropillars improved the mechanical robustness of the WHS [31].

Fig. 1c shows a schematic illustration and an inclined-view SEM image of the fabricated morphology-controllable WHS, with the details of the fabrication process and the results of each step explained in Figs. S1 and S2. The final WHS comprised a complex of micropatterns, nanopatterns, and wrinkles, and the morphology of each structure could

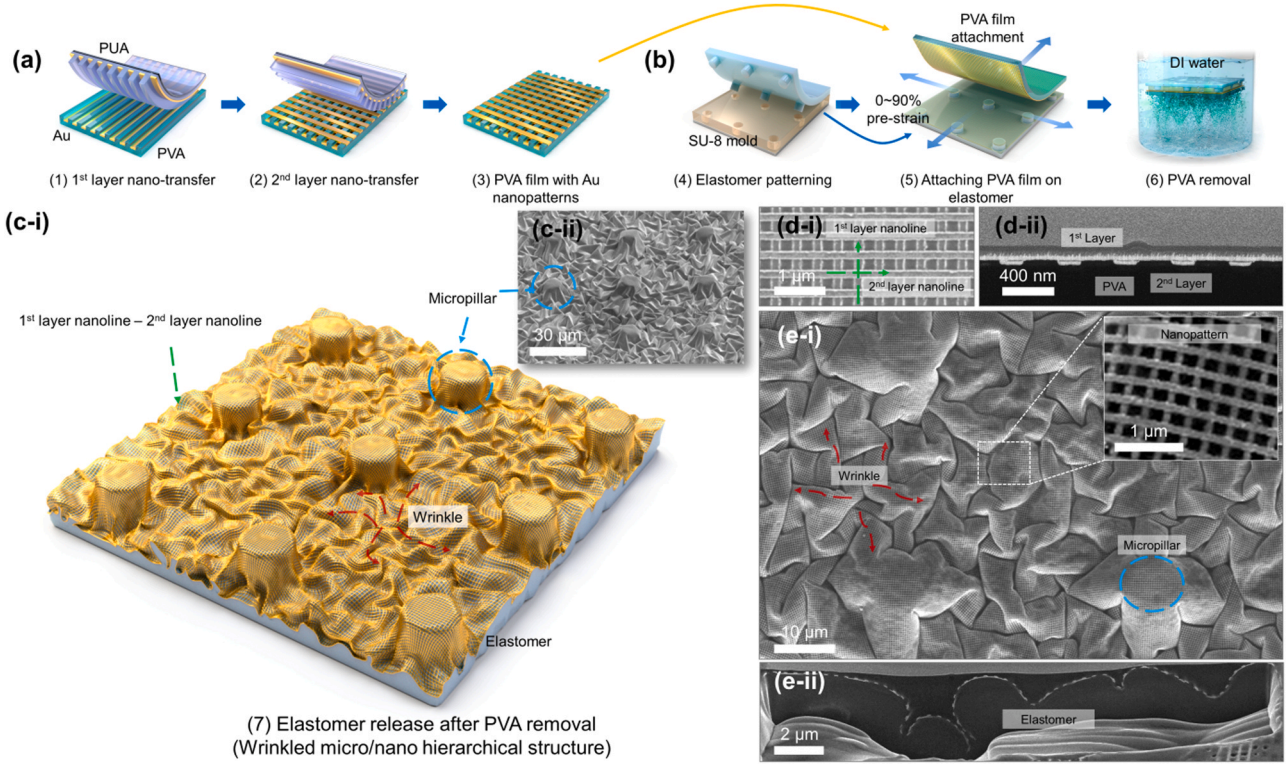


Fig. 1. Schematic of fabrication process of the morphology-controllable wrinkled micro/nano hierarchical structure (WHS) and scanning electron microscopy (SEM) images of fabricated structure. (a) Nanotransfer of nanopatterns onto the water-soluble film. (b) Elastomer molding and integration of nanopatterns, micropatterns, and wrinkles: Multilayered nanopatterns were transferred onto a pre-strained micropatterned elastomer, and the water-soluble film was dissolved. (c-i) Schematics and (c-ii) inclined-view SEM image of the fabricated WHS. (d-i) Top-view and (ᴅ-ii) side-view SEM images of the transferred multilayered nanopatterns on the water-soluble film. (e-i) Top view and (e-ii) side view SEM images of the fabricated WHS on the elastomer substrate.

be individually controlled. Fig. 1d shows the top and side SEM views of well-aligned nanopatterns on the PVA film before attachment to the elastomer. These multilayered nanostructures composed of the first- and second-layer nanolines maintained their original mesh shape during the fabrication process (Fig. 1e-i). In addition, irregular and highly dense wrinkles were successfully formed between the micropillars of the elastomer substrate, as shown in Fig. 1e-ii.

3.2. Effect of fabrication parameters on the WHS surface morphology

As discussed in Section 3.1, the developed fabrication process allowed not only the integration of nanopatterns, micropatterns, and wrinkles, but also the control of individual structures. Fig. 2 shows SEM images of diverse WHS surface morphologies for different nanopatterns, micropatterns, and wrinkles, with detailed structural information presented in Table S1. As a first controllable parameter, multilayered nanopatterns (including film, line–line, dot–line–line, and line–line–dot patterns) were independently fabricated on the PVA films (Fig. S5) and transferred onto the elastomer. When an Au film (without pattern) was applied to the PVA film, the micropillars were not observed because of the high bending stiffness of the Au film even at a low thickness of 40 nm. However, when multilayered nanopatterns were transferred, the micropillars and nanopatterns retained their original shapes (Fig. 2a). This method of 3D nanopattern transfer allowed an unlimited number of nanostructure designs to be obtained by variation of each layer. The micropatterns could also be varied via a photolithographic patterning process.

Several nanostructure designs with different pre-strain and micropattern spacing were investigated. First, the micropattern shape was fixed as an array of 10-μm-diameter pillars, and the spacing between them was varied between 10 and 40 μm to verify the relationship between micropatterns and wrinkles. Larger spacings allowed more wrinkles to be formed between pillars (Fig. 2b-i), while overly narrow spacings caused the wrinkles to cover the micropillars (Fig. S6). Second, the micropattern shape was changed from micropillar to micropyramid, and the size of the micropattern was varied between 10 and 50 μm to verify the design diversity of the micropattern. As the size of the micropyramids increased, the nanopatterns adhered to the pyramids conformally (Fig. 2b-ii). Finally, the wrinkles were controlled by the degree of pre-strain. When nanopatterns were transferred without pre-

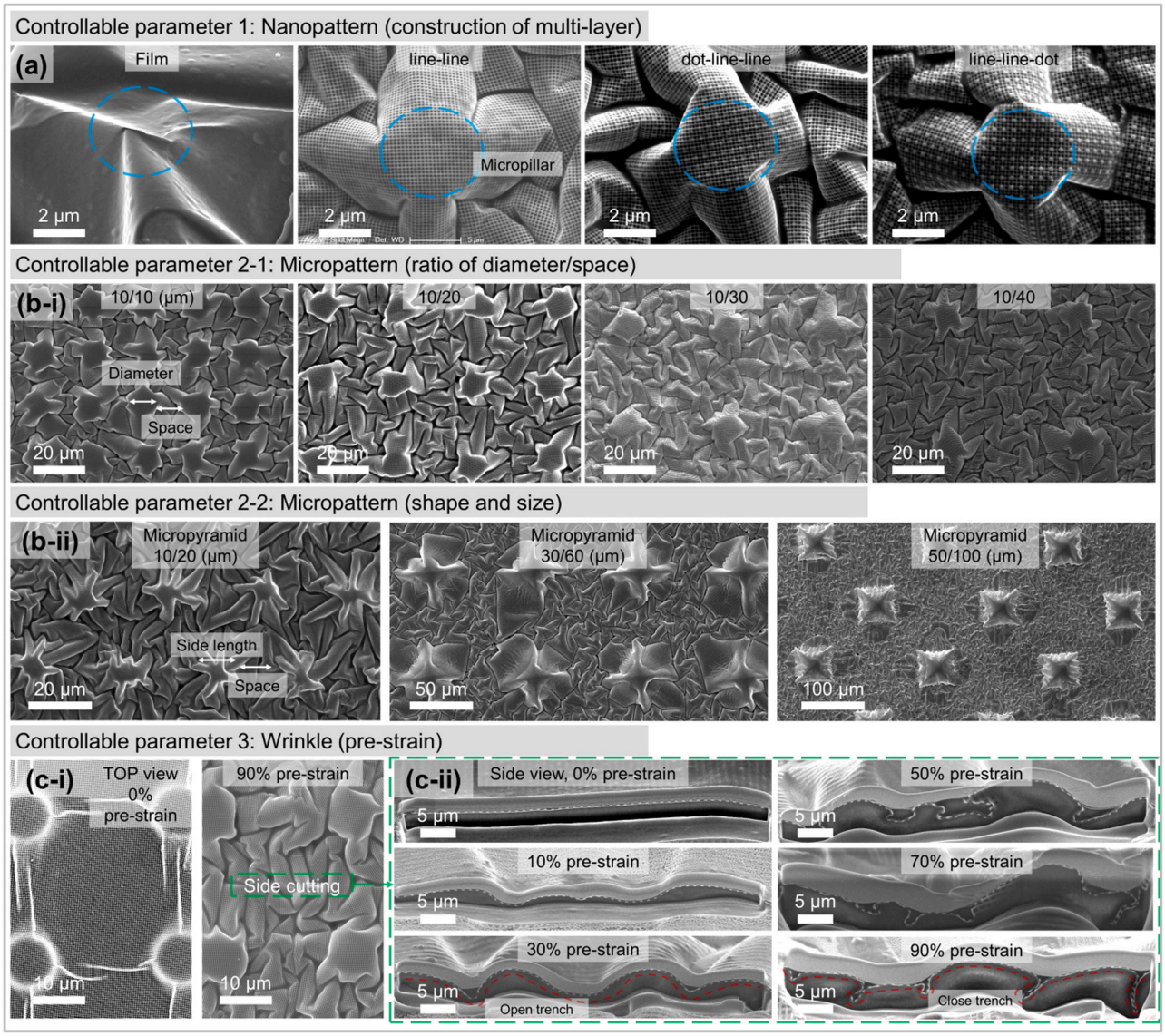


Fig. 2. SEM images of diverse WHSs with different nanopatterns, micropatterns, and wrinkles demonstrating the design diversity and shape controllability of surface morphology. SEM images of the WHS with (a) various multilayered nanopatterns, (b-i) different ratios between the diameter and spacing and (b-ii) shape and size of micropatterns, and (c) different pre-strains as controllable parameters. (c-i) Top view of the WHS and (c-ii) side view of wrinkles between micropatterns.

straining, the mesh nanopatterns conformally covered the elastomer without any wrinkles (Fig. 2c-i, left image). On the other hand, several multiscale wrinkles were generated under 90% pre-strain (Fig. 2c-i, right image). Notably, the density of wrinkles increased with increasing pre-strain, although a closed trench that made the surface relatively flat was obtained at an excessively large pre-strain (Fig. 2c-ii). In other words, even though the density of wrinkles under 90% pre-strain exceeded that under 50% pre-strain, the effective surface area and roughness were larger in the latter case (Fig. S7). Therefore, when designing a hierarchical structure, one should choose a pre-strain and micropattern spacing optimally suited for the target application.

3.3. Contact angle analysis

Hydrophobicity is an essential property for TENG devices because it enables them to work as self-powered sensors and energy harvesting devices with humidity-resistant, contamination-resistant, and self-cleaning effects [32]. Since the developed WHS featured a large surface area and high roughness, which are the most essential features of hydrophobic surfaces and TENGs, it was used to fabricate an S-TENG.

First, contact angle measurements were performed to evaluate the wettability of the WHS. A flat Au film without any micro/nanostructures exhibited a contact angle of $93.8 \pm 0.5°$, which increased to $101.4 \pm 0.7°$ in the case of line–line nanopatterns and to $103.4 \pm 0.3°$ in the case of line–line–dot nanopatterns (Fig. 3a). This behavior originated from the large surface area and high roughness at the nanoscale. According to Wenzel's wetting theory, the contact angle of a hydrophobic surface can be increased by surface roughening because of the concomitant increase in surface area [18]. This effect was achieved herein by the application of multilayered nanopatterns, and wrinkled structures were added to the elastomer substrate with line–line–dot nanopatterns.

As shown in Fig. 3b, the apparent contact angle increased with increasing pre-strain within the small pre-strain range (0–50%), whereas the opposite tendency was observed within the large pre-strain range (50–90%). As discussed in Fig. 2, the effective surface area and roughness decreased under extremely large pre-strain owing to the presence of closed trenches. Therefore, the apparent contact angle (and thus, effective surface roughness) was maximized at $137.6 \pm 0.5°$ under the pre-strain of 50%. Additionally, according to the Cassie–Baxter model, air can be trapped at the droplet–substrate interface in the case of a highly complex surface, which results in a higher apparent contact angle [18]. In wrinkled structures with nanopatterns, the Wenzel state can co-exist with the Cassie–Baxter state, or an intermediate state can be generated (Fig. S8) [33]. Therefore, the addition of wrinkles with the optimized pre-strain to nanopatterns can significantly increase the contact angle because of the formation of a sophisticated surface.

Subsequently, we investigated how the wettability was affected by the addition of micropatterns to the wrinkled and nanopatterned surface. Interestingly, the contact angle decreased to $127.2 \pm 0.6°$ for the micropattern with a 10-μm spacing but increased to $152.5 \pm 1.3°$ with a 30-μm spacing (Fig. 3c), decreasing again when the spacing further increased to 40 μm. This result is believed to reflect two WHS characteristics. (i) Dense micropatterns hinder the formation of wrinkles, and the wrinkled structure can exhibit a much larger contact angle than the micropatterned structure. This behavior originates from the fact that dense and multiscale wrinkles can produce a state that is intermediate between the Cassie–Baxter and Wenzel states, whereas the micropattern itself is in the Wenzel state. (ii) In the intermediate state, an increase in the aspect ratio of the surface structure can improve hydrophobicity [34]. Therefore, the addition of micropatterns with a proper pattern spacing increases the WHS aspect ratio and, thus, the contact angle. A detailed description of the above reasoning is presented in Fig. S8. Therefore, a parametric study was conducted to improve the WHS hydrophobicity, and the results demonstrated that the developed WHS can be used as a superhydrophobic surface.

3.4. Effect of WHS on the TENG characteristics

As TENG performance can be improved by increasing the roughness and surface area [8,35–37], it was reasonably expected that the developed WHS can be used to fabricate a high-performance TENG. To verify the effects of the WHS on the corresponding TENG, a contact-separation-mode device was fabricated and analyzed. To maximize the triboelectric effects, WHS Au nanopatterns were used as the positive triboelectric materials, while PFPE was used as the negative triboelectric material (Fig. 4a) [38]. When the two oppositely charged surfaces are brought into contact, electrons move from the positive material to the negative material, and the open-circuit voltage increases with increasing distance between the surfaces. A detailed description of TENG principles is shown in Fig. S9. Based on this mechanism, we evaluated the WHS TENG characteristics as functions of surface morphology, with the experimental setup shown in Fig. S3.

The open-circuit voltage of the TENG with a flat Au film and flat PFPE equaled 7.9 V, whereas a higher value of 13.6 V was obtained when the flat PFPE film was replaced by nanopatterned PFPE. In addition, the voltage increased to 16.5 V as the flat Au film was replaced by a line–line–dot nanopattern. This improvement originates from the well-known roughening effect of nanopatterns [39]. Notably, the tendency of nanopattern-induced improvement was identical to that observed for the contact angle, which implies that the line–line–dot nanopattern has the highest surface roughness among the patterns used herein, thus inducing the maximal improvement of open-circuit voltage output.

When wrinkles were added to nanopatterns, the voltage output of the TENG increased to a maximum of 35.9 V when 70% pre-strain was used, which contrasted with the results of contact angle analysis, wherein the

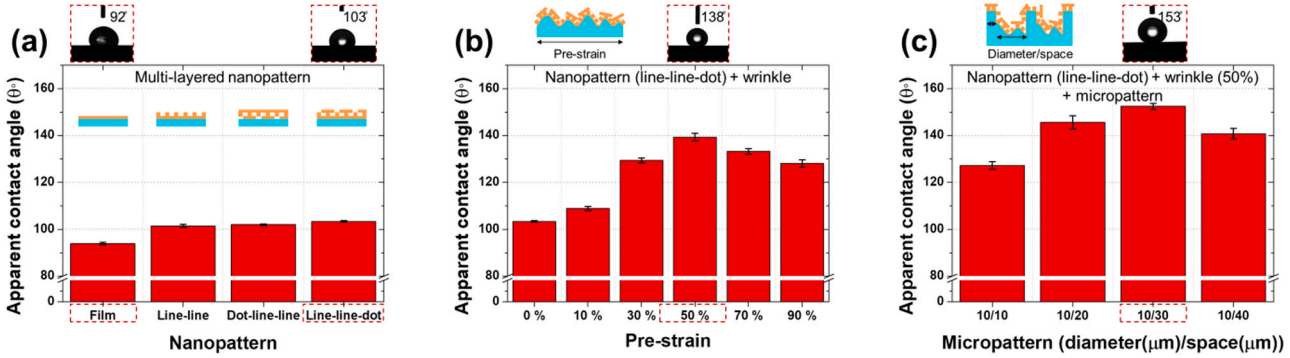


Fig. 3. Results of contact angle analysis. Effects of (a) nanopatterns, (b) adding wrinkles to the nanopatterns, and (c) adding micropatterns to the wrinkles with nanopatterns. The structures were sequentially added to the flat elastomer substrate to verify the effects of each added structure. For these experiments, to measure the contact angle, a 10-μm droplet of DI water was placed on the surface of each sample.

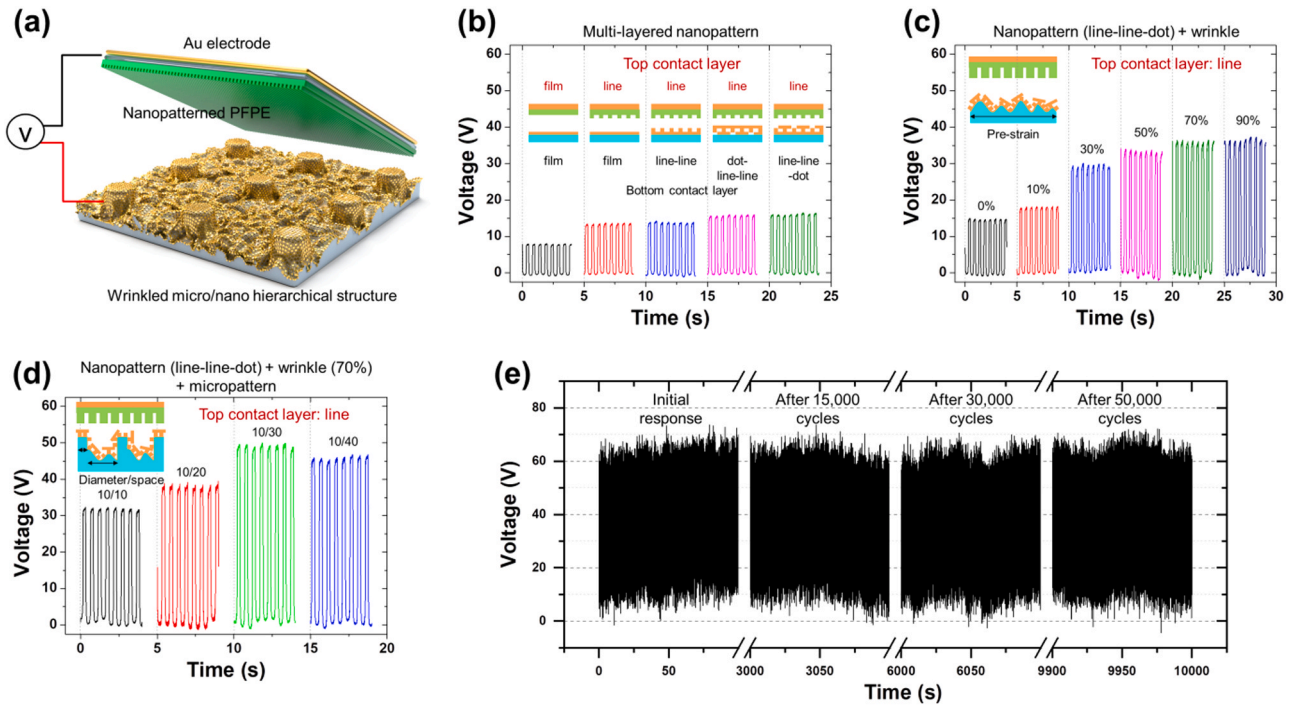


Fig. 4. S-TENG characterization. (a) Schematics of the developed TENG. Dependence of open-circuit voltage on (b) nanopatterns, (c) wrinkles, and (d) micropatterns. The structures were sequentially added to the flat elastomer substrate to verify the effects of each added structure. For these experiments, the TENG was vibrated using a 2-Hz input signal during the whole experiment. (e) The results of 50,000 cyclic stability tests under a vibration input of 5 Hz. The measured voltage refers to the open-circuit voltage.

maximum contact angle was obtained with 50% pre-strain. In the TENG, the closed trenches could be stretched under applied pressure during operation, which enhanced the voltage output. In contrast, during contact angle analysis, these trenches flattened the surface, reducing the apparent contact angle. Therefore, the dense wrinkles at 70% pre-strain were beneficial for the TENG, even though they were detrimental to the wettability.

Finally, when micropillars were added to the wrinkled structure with nanopatterns, the TENG performance was maximized for a spacing of 30 μm. The maximized output voltage of 48.0 V exceeded that of the flat TENG by 608%. In a TENG with uniform micropatterns, the triboelectric charges are more easily separated to facilitate the formation of a larger dipole moment between the electrodes [40]. However, overly dense micropatterns hinder the formation of wrinkles, as observed in the contact angle analysis. Therefore, the above results suggest that the S-TENG composite structure of wrinkles at 50% pre-strain, line–line–dot nanopatterns, and micropatterns with a 30 μm spacing is optimal.

The developed WHS also showed superior mechanical robustness. The optimized TENG maintained its performance after 50,000 cycles of repeated contact–release motions (Fig. 4e) and was concluded to be suitable for applications (such as energy harvesting and self-powered sensing) requiring a long lifetime and even repeated pressure. Other detailed parameters of the produced TENG, including the effects of frequency, charge density, and force, are presented in Fig. S10.

3.5. Characterization of the S-TENG

A water spraying experiment was conducted to characterize the water-repellence of the WHS in the S-TENG. In most hydrophobic TENGs, only the negative triboelectric substrate can be made hydrophobic (Table S2), as the common negative materials such as Teflon and polydimethylsiloxane (PDMS) show inherent hydrophobicity. On the other hand, the positive triboelectric substrate is generally hydrophilic, as positive materials such as fabrics and metals are inherently hydrophilic. Therefore, it has been challenging to make both TENG substrates hydrophobic. However, in our S-TENG, the positive triboelectric substrate (i.e., the developed WHS) exhibited superhydrophobicity due to its very rough surface, as discussed in Section 3.3. In addition, the negative triboelectric material (PFPE) is inherently hydrophobic, and its hydrophobicity could be enhanced by nanopatterning to achieve superhydrophobicity. Thus, an entirely superhydrophobic TENG was fabricated and characterized, with the negative triboelectric substrate fixed as the superhydrophobic nanopatterned PFPE (Fig. S11).

For comparison, a TENG with an Au film electrode was fabricated. The open-circuit voltage of this Au film TENG equaled 12.5 V in air but decreased to almost 0 V immediately after water spraying. This behavior was ascribed to the fact that the triboelectric effect rarely occurs in humid environments, as transferred electrons can escape from the surface to the droplets [41]. The noise-level output lasted 50 min, and the voltage subsequently recovered as the water naturally evaporated (Fig. 5a). The peak voltage signal of one recovery step (step 1) cycle, which indicates the released-state voltage, decreased with time, while those of the initial and recovered states were maintained (Fig. 5b). In the released state of step 1, the transferred electrons escaped to the locally remaining droplets at the surface, which resulted in a voltage drop.

For the S-TENG comprising the superhydrophobic WHS as a positive triboelectric substrate, the voltage output in air (48.0 V) was 3.84 times higher than that of the Au film TENG. After water spraying, the voltage decreased to the noise level but rapidly recovered within 50 s, as the droplets spread out toward the outside of the TENG surface (Fig. 5c). Notably, unlike the TENG with a single hydrophobic surface, which recovered gradually, a step function-type recovery was observed for the S-TENG, because in the latter case, the droplets bounced off before naturally evaporating (Fig. S12). The superhydrophobicity of both TENG surfaces allowed the droplets to gather in a spherical shape and be expelled. In addition, despite the presence of abundant droplets on the surface, the S-TENG had locally water-free regions owing to the gathered droplets. Therefore, a sharp voltage output occurred in recovery step 1, as the electrons rapidly escaped into the droplets after being transferred through the water-free region (Fig. 5d). In conclusion, the S-

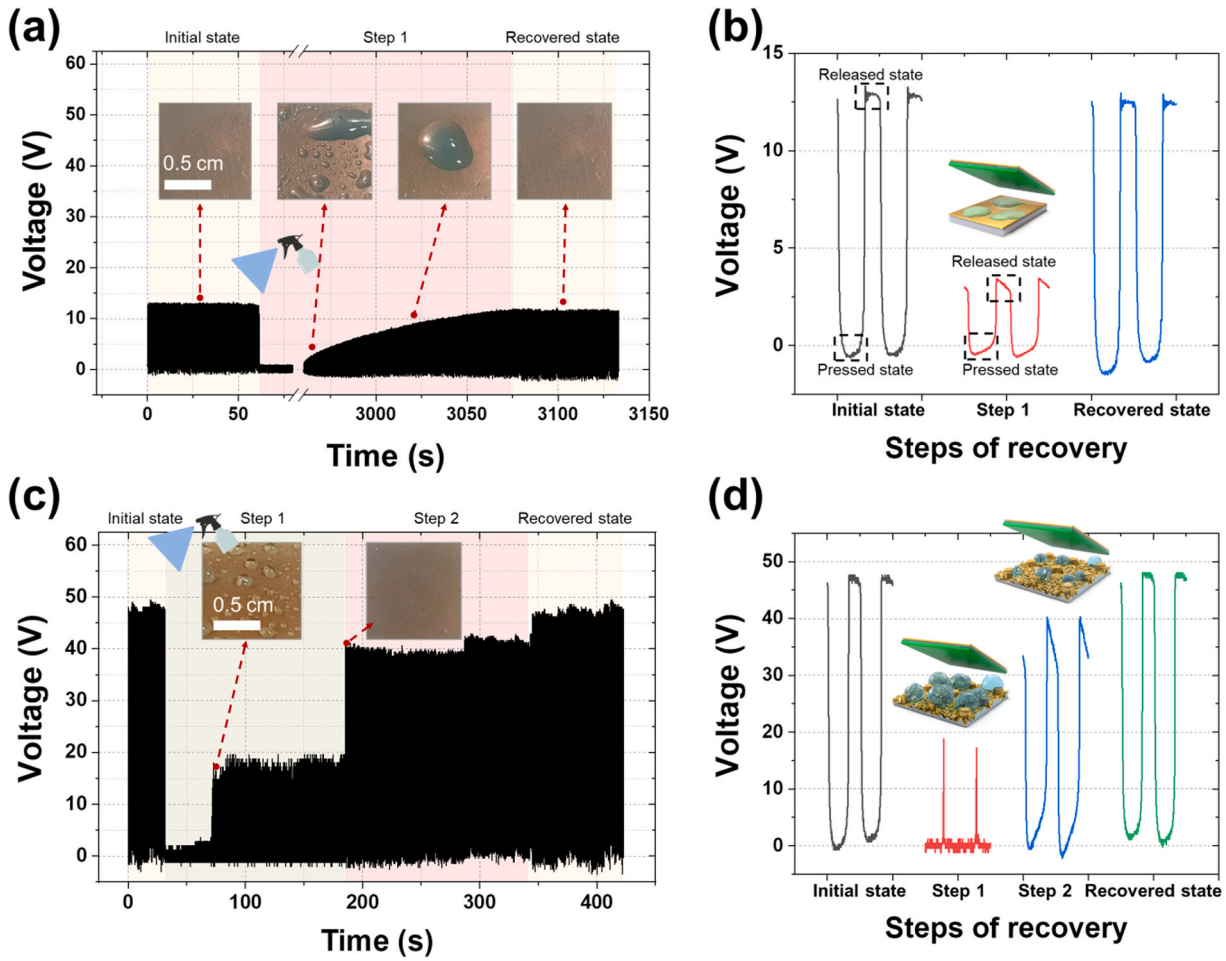


Fig. 5. Effects of the superhydrophobic surface on the TENG performance. (a) Results of the water spraying test for the Au film TENG and (b) enlarged graph showing the effect of the recovery step on the shape of the voltage recovery curve. (c) Results of water spraying test obtained for the S-TENG and (d) enlarged graph showing the effect of the recovery step on the shape of the voltage recovery curve. Water was sprayed at a specific time during TENG vibration under an input signal of 4 Hz. The measured voltage refers to the open-circuit voltage.

TENG, which had two superhydrophobic surfaces, showed a ten-fold faster recovery than the conventional TENG with a single superhydrophobic surface.

3.6. Application of S-TENG to self-powered water-repellent cough detection sensor

The practical utility of the S-TENG was demonstrated by its application as a self-powered and water-repellent cough detection sensor. Cough is the most common reason for patients to seek medical advice from general practitioners, pediatricians, and neurologists [42], and is a distressing symptom that results in significant healthcare costs, medical consultations, and medication use [43]. More significantly, droplet infection caused by coughing is a representative cause of the increasing transmission rates of epidemics such as COVID-19 [44] and the bubonic plague [45]. Therefore, the detection of coughing patients or members of public is important for improving the quality of life.

Previously reported cough detection sensors employ microphones, which cannot detect individual cough signals or be used in noisy environments [42,46]. In addition, other wearable pressure sensors attached to the mask can be affected by droplets originating from coughing or the external environment, as their working principle is based on a change in resistance or capacitance and they usually do not have hydrophobic surfaces [47–49]. Furthermore, these pressure sensors inevitably require a power source because typical resistive-type and capacitive-type sensors require the supply of voltage or current to read electric signal changes of the devices [50,51]; thus, self-powered sensors are becoming an essential element of wearable sensors, as they can operate for a long time without requiring an external power source. To the best of our knowledge, the development of self-powered and water-repellent cough detection sensors for individual cough detection remains a challenge. Therefore, we utilized the developed S-TENG as a self-powered and water-repellent cough detection sensor. TENG-based sensors are considered self-powered sensors because the device itself generates electrical signals by external stimuli without any external power consumption [52].

To prepare the TENG-based cough detection sensor, the positive triboelectric substrate was attached to the outer layer of a reusable mask, and the negative triboelectric substrate was attached to the exhalation valve on the inner layer of the mask (Fig. 6a). During exhalation, the airflow opens the exhalation valve and presses the TENG, whereas during inhalation, air enters through the filters next to the exhalation valve, which closes the valve and releases the pressure on the TENG.

When the sensor was prepared using the Au film TENG, the responses of the pressure sensor to coughing and strong exhalation equaled 1–6 and 1 V, respectively, whereas the response to shouting could not be distinguished from noise (Fig. 6b). Even though the coughing signal was distinguishable from other signals, the sensor response to coughing rapidly decreased to 0.2 V upon water spraying (Fig. 6c). The sprayed droplets remained on the TENG surface, as only the nanopatterned PFPE (and not both substrates) was hydrophobic.

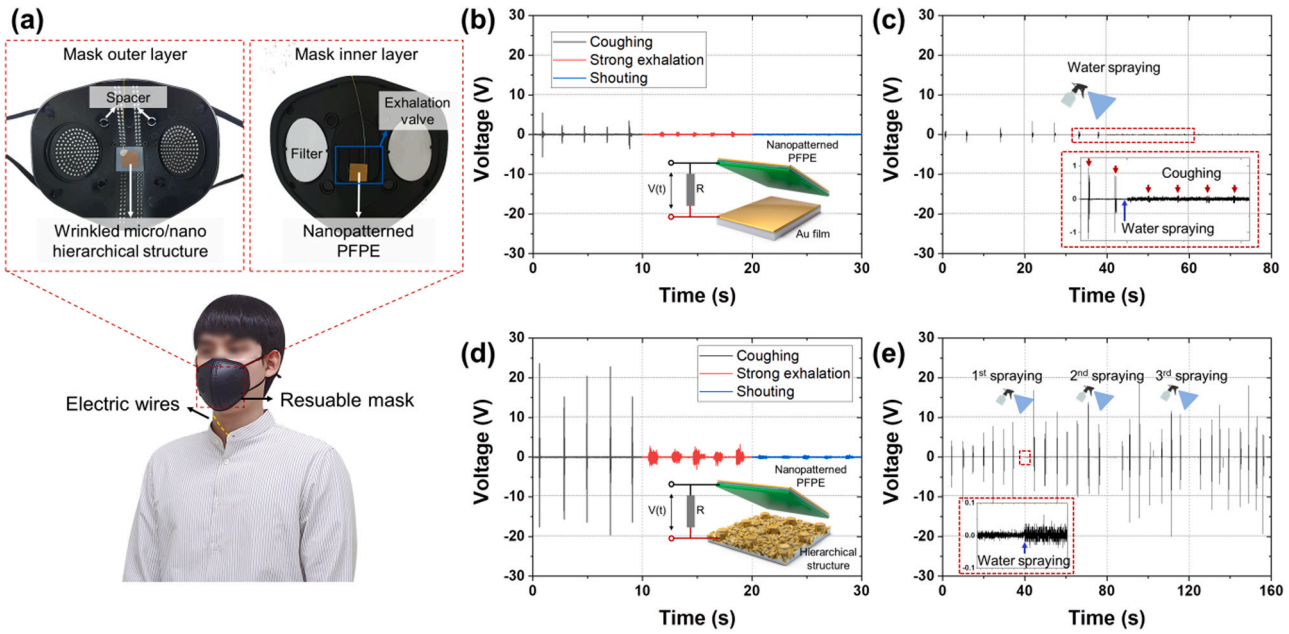


Fig. 6. Application of the S-TENG as a self-powered and water-repellent cough detection sensor. (a) Photograph of a reusable mask with the cough detection sensor. In the sensor, the positive triboelectric substrate was attached to the outer layer of the reusable mask, and the negative triboelectric substrate was attached to an exhalation valve of the mask inner layer. The outer layer of the mask was separated from the inner layer by spacers. (b) Sensor responses to coughing, strong exhalation, and shouting. (c) Output voltage-time curve recorded for coughing, with water sprayed at a specific time. (d), (e) Results obtained when the same experiments were conducted with the S-TENG. All the load resistors used in these experiments were 10 MΩ.

On the other hand, the sensor prepared using the developed S-TENG had responses of 5–24, 3, and 1 V upon coughing, strong exhalation, and shouting, respectively, as shown in Fig. 6d and Video 1. Thus, the S-TENG had an approximately five-fold higher sensitivity than the Au film TENG owing to the very rough surface of the former. Furthermore, as both substrates of the S-TENG were superhydrophobic, sprayed water droplets and droplets generated by coughing were rapidly expelled from the TENG under the force of gravity. The developed sensor maintained its performance without response degradation even after being sprayed with water three times (Fig. 6e and Video 2). Therefore, it was concluded that the self-powered and water-repellent cough detection sensor based on the developed S-TENG exhibits high sensitivity to coughing and superior water repellency.

Supplementary material related to this article can be found online at doi:10.1016/j.nanoen.2021.105978.

4. Conclusions

A morphology-controllable wrinkled micro/nano hierarchical structure was developed by integrating micropatterns, nanopatterns, and wrinkles on a single substrate using a novel fabrication method combining nanotransfer, molding, and the buckling effect, which allowed independent control of the three different structures in the WHS. As this method allows each structure to be controlled individually, it offers unlimited design diversity. Additionally, to apply the fabricated WHS as an S-TENG, we investigated the surface hydrophobicity and triboelectric effects. The very rough surface of the WHS enhanced the hydrophobicity and triboelectric effect; specifically, a superior contact angle of 152.5° and a 608% enhancement of triboelectric effects compared to the film-based TENG were observed. Furthermore, the S-TENG was utilized as a self-powered and water-repellent cough detection sensor that had an entirely superhydrophobic structure and maintained superior detection performance during repeated spraying with water owing to its hierarchical structure. To the best of our knowledge, this study is the first attempt of integrating three types of structures (micropatterns, nanopatterns, and wrinkles) onto a single substrate and is therefore a benchmark for subsequent research. Furthermore, the proposed structure and fabrication methods are expected to contribute to the use of hierarchical structures in broader and real-life applications such as catalysts, energy harvesting, chemical sensing, contact angle engineering, and biomedical devices.

CRediT authorship contribution statement

Junseong Ahn: Conceptualization, Methodology, Visualization. **Zhi-Jun Zhao:** Methodology, Visualization. **Jungrak Choi:** Software. **Yongrok Jeong:** Conceptualization. **Soonhyoung Hwang:** Writing - original draft. **Jiwoo Ko:** Methodology, Forman analysis. **Jimin Gu:** Methodology. **Sohee Jeon:** Validation. **Jaeho Park:** Validation. **Mingu Kang:** Software. **Dionisio V. Del Orbe:** Writing - original draft, Writing - review & editing. **Incheol Cho:** Validation, Visualization. **Hyeokjung Kang:** Software, Validation. **Moonjeong Bok:** Methodology. **Jun-Ho Jeong:** Supervision. **Inkyu Park:** Supervision.

Declaration of Competing Interest

The authors declare that they have no known competing financial interests or personal relationships that could have appeared to influence the work reported in this paper.

Acknowledgements

Funding: This work was supported by the Center for Advanced Meta-Materials (CAMM) funded by the Ministry of Science, ICT and Future Planning, Korea, through the Global Frontier Project [CAMM-No. 2014M3A6B3063707] (25%); and the Basic Research Program of KIMM (Korea Institute of Machinery and Materials, NK230C) (25%); and a National Research Foundation of Korea (NRF) grant funded by the Korea government (MSIT) [No. 2021R1A2C3008742] (50%).

Appendix A. Supporting information

Supplementary data associated with this article can be found in the online version at doi:10.1016/j.nanoen.2021.105978.

References

[1] R.S. Lakes, Materials with a structural hierarchy, Nature 361 (1993) 511–515, https://doi.org/10.1038/361511a0.

[2] H.K. Raut, A. Baji, H.H. Hariri, H. Parveen, G.S. Soh, H.Y. Low, K.L. Wood, Gecko-inspired dry adhesive based on micro-nanoscale hierarchical arrays for application in climbing devices, ACS Appl. Mater. Interfaces 10 (2018) 1288–1296, https://doi.org/10.1021/acsami.7b09526.

[3] Y. Xiu, Y. Liu, D.W. Hess, C.P. Wong, Mechanically robust superhydrophobicity on hierarchically structured Si surfaces, Nanotechnology 21 (2010), 155705, https://doi.org/10.1088/0957-4484/21/15/155705.

[4] A.Y.Y. Ho, L.P. Yeo, Y.C. Lam, I. Rodríguez, Fabrication and analysis of gecko-inspired hierarchical polymer nanosetae, ACS Nano 5 (2011) 1897–1906, https://doi.org/10.1021/nn103191q.

[5] S.S. Latthe, C. Terashima, K. Nakata, A. Fujishima, Superhydrophobic surfaces developed by mimicking the hierarchical surface morphology of lotus leaf, Molecules 19 (2014) 4256–4283, https://doi.org/10.3390/molecules19044256.

[6] H. Gao, D. Wei, P. Lin, C. Liu, P. Sun, K. Shimanoe, N. Yamazoe, G. Lu, The design of an excellent xylene gas sensor using a Sn-doped NiO hierarchical nanostructure, Sens. Actuators B 253 (2017) 1152–1162, https://doi.org/10.1016/j.snb.2017.06.177.

[7] Y. Song, W. Wang, L. Ge, X. Xu, Z. Zhang, P.S.B. Julião, W. Zhou, Z. Shao, Rational design of a water-storable hierarchical architecture decorated with amorphous barium oxide and nickel nanoparticles as a solid oxide fuel cell anode with excellent sulfur tolerance, Adv. Sci. 4 (2017), 1700337, https://doi.org/10.1002/advs.201700337.

[8] H. Kang, C. Zhao, J. Huang, D.H. Ho, Y.T. Megra, J.W. Suk, J. Sun, Z.L. Wang, Q. Sun, J.H. Cho, Fingerprint-inspired conducting hierarchical wrinkles for energy-harvesting E-skin, Adv. Funct. Mater. 29 (2019), 1903580, https://doi.org/10.1002/adfm.201903580.

[9] J.H. Lee, H.W. Ro, R. Huang, P. Lemaillet, T.A. Germer, C.L. Soles, C.M. Stafford, Anisotropic hierarchical surface patterns via surface wrinkling of nanopatterned polymer films, Nano Lett. 12 (2012) 5995–5999, https://doi.org/10.1021/nl303512d.

[10] W.B. Jung, G.T. Yun, Y. Kim, M. Kim, H.T. Jung, Relationship between hydrogen evolution and wettability for multiscale hierarchical wrinkles, ACS Appl. Mater. Interfaces 11 (2019) 7546–7552, https://doi.org/10.1021/acsami.8b19828.

[11] C. Yang, C. Zhao, X. Wang, M. Shi, Y. Zhu, L. Jing, C. Wu, J. Chang, Stimulation of osteogenesis and angiogenesis by micro/nano hierarchical hydroxyapatite via macrophage immunomodulation, Nanoscale 11 (2019) 17699–17708, https://doi.org/10.1039/C9NR05730G.

[12] Y. Tian, L. Jiang, Intrinsically robust hydrophobicity, Nat. Mater. 12 (2013) 291–292, https://doi.org/10.1038/nmat3610.

[13] J. Henzie, M.H. Lee, T.W. Odom, Multiscale patterning of plasmonic metamaterials, Nat. Nanotechnol. 2 (2007) 549–554, https://doi.org/10.1038/nnano.2007.252.

[14] B. Dudem, Y.H. Ko, J.W. Leem, J.H. Lim, J.S. Yu, Hybrid energy cell with hierarchical nano/micro-architectured polymer film to harvest mechanical, solar, and wind energies individually/simultaneously, ACS Appl. Mater. Interfaces 8 (2016) 30165–30175, https://doi.org/10.1021/acsami.6b09785.

[15] A.M. Brzozowska, S. Maassen, R.G.Z. Rong, P.I. Benke, C.-S. Lim, E.M. Marzinelli, D. Jańczewski, S.L.-M. Teo, G.J. Vancso, Effect of variations in micropatterns and surface modulus on marine fouling of engineering polymers, ACS Appl. Mater. Interfaces 9 (2017) 17508–17516, https://doi.org/10.1021/acsami.6b14262.

[16] W.K. Lee, W.B. Jung, S.R. Nagel, T.W. Odom, Stretchable superhydrophobicity from monolithic, three-dimensional hierarchical wrinkles, Nano Lett. 16 (2016) 3774–3779, https://doi.org/10.1021/acs.nanolett.6b01169.

[17] J. Choi, W. Cho, Y.S. Jung, H.S. Kang, H.T. Kim, Direct fabrication of micro/nano-patterned surfaces by vertical-directional photofluidization of azobenzene materials, ACS Nano 11 (2017) 1320–1327, https://doi.org/10.1021/acsnano.6b05934.

[18] J. Choi, W. Jo, S.Y. Lee, Y.S. Jung, S.H. Kim, H.T. Kim, Flexible and robust superomniphobic surfaces created by localized photofluidization of azopolymer pillars, ACS Nano 11 (2017) 7821–7828, https://doi.org/10.1021/acsnano.7b01783.

[19] Y. Xue, W.K. Lee, J. Yuan, T.W. Odom, Y. Huang, Mechanics modeling of hierarchical wrinkle structures from the sequential release of prestrain, Langmuir 34 (2018) 15749–15753, https://doi.org/10.1021/acs.langmuir.8b03498.

[20] W.B. Jung, K.M. Cho, W.K. Lee, T.W. Odom, H.T. Jung, Universal method for creating hierarchical wrinkles on thin-film surfaces, ACS Appl. Mater. Interfaces 10 (2018) 1347–1355, https://doi.org/10.1021/acsami.7b14011.

[21] W.K. Lee, T.W. Odom, Designing hierarchical nanostructures from conformable and deformable thin materials, ACS Nano 13 (2019) 6170–6177, https://doi.org/10.1021/acsnano.9b03862.

[22] S. Schauer, M. Worgull, H. Hölscher, Bio-inspired hierarchical micro- and nano-wrinkles obtained via mechanically directed self-assembly on shape-memory polymers, Soft Matter 13 (2017) 4328–4334, https://doi.org/10.1039/C7SM00154A.

[23] D. Wang, N. Cheewaruangroj, Y. Li, Mc.G. Hale, Y. Jiang, D. Wood, J.S. Biggins, B. B. Xu, Spatially configuring wrinkle pattern and multiscale surface evolution with structural confinement, Adv. Funct. Mater. 28 (2018), 1704228, https://doi.org/10.1002/adfm.201704228.

[24] S.H. Hwang, Z.-J. Zhao, S. Jeon, H. Kang, J. Ahn, J.-H. Jeong, Repeatable and metal-independent nanotransfer printing based on metal oxidation for plasmonic color filters, Nanoscale 11 (2019) 11128–11137, https://doi.org/10.1039/C9NR00176J.

[25] J. Ko, Z.-J. Zhao, S.-H. Hwang, H.-J. Kang, J. Ahn, S. Jeon, M. Bok, Y. Jeong, K. Kang, I. Cho, J.-H. Jeong, I. Park, Nanotransfer printing on textile substrate with water-soluble polymer nanotemplate, ACS Nano 14 (2020) 2191–2201, https://doi.org/10.1021/acsnano.9b09082.

[26] Z.-J. Zhao, J. Ko, J. Ahn, M. Bok, M. Gao, S.H. Hwang, H.-J. Kang, S. Jeon, I. Park, J.-H. Jeong, 3D layer-By-layer Pd-containing nanocomposite platforms for enhancing the performance of hydrogen sensors, ACS Sens. 5 (2020) 2367–2377, https://doi.org/10.1021/acssensors.0c00211.

[27] Z.-J. Zhao, J. Ahn, S.H. Hwang, J. Ko, Y. Jeong, M. Bok, H.-J. Kang, J. Choi, S. Jeon, I. Park, J.-H. Jeong, Large-area nanogap-controlled 3D nanoarchitectures fabricated via layer-by-layer nanoimprint, ACS Nano 15 (2021) 503–514, https://doi.org/10.1021/acsnano.0c05290.

[28] Z.-J. Zhao, J. Ahn, J. Ko, Y. Jeong, M. Bok, S.H. Hwang, H.-J. Kang, S. Jeon, J. Choi, I. Park, J.-H. Jeong, Shape-controlled and well-arrayed heterogeneous nanostructures via melting point modulation at the nanoscale, ACS Appl. Mater. Interfaces 13 (2021) 3358–3368, https://doi.org/10.1021/acsami.0c18122.

[29] Z.-J. Zhao, S.H. Hwang, H.-J. Kang, S. Jeon, M. Bok, S. Ahn, D. Im, J. Hahn, H. Kim, J.-H. Jeong, Adhesive-layer-free and double-faced nanotransfer lithography for a flexible large-area metasurface hologram, ACS Appl. Mater. Interfaces 12 (2020) 1737–1745, https://doi.org/10.1021/acsami.9b14345.

[30] Y. Xue, W.-K. Lee, J. Yuan, T.W. Odom, Y. Huang, Mechanics modeling of hierarchical wrinkle structures from the sequential release of prestrain, Langmuir 34 (2018) 15749–15753, https://doi.org/10.1021/acs.langmuir.8b03498.

[31] M. Agostini, G. Greco, M. Cecchini, Polydimethylsiloxane (PDMS) irreversible bonding to untreated plastics and metals for microfluidics applications, APL Mater. 7 (2019), 081108, https://doi.org/10.1063/1.5070136.

[32] Q. Zhou, K. Lee, K.N. Kim, J.G. Park, J. Pan, J. Bae, J.M. Baik, T. Kim, High humidity- and contamination-resistant triboelectric nanogenerator with superhydrophobic interface, Nano Energy 57 (2019) 903–910, https://doi.org/10.1016/j.nanoen.2018.12.091.

[33] D. Murakami, H. Jinnai, A. Takahara, Wetting transition from the Cassie-Baxter state to the Wenzel state on textured polymer surfaces, Langmuir 30 (2014) 2061–2067, https://doi.org/10.1021/la4049067.

[34] M.A. Rahman, A.M. Jacobi, Experimental investigation of wetting anisotropy on microgrooved brass surfaces, Procedia Eng. 90 (2014) 611–617, https://doi.org/10.1016/j.proeng.2014.11.780.

[35] Z. Wen, Y. Yang, N. Sun, G. Li, Y. Liu, C. Chen, J. Shi, L. Xie, H. Jiang, D. Bao, Q. Zhuo, X. Sun, A wrinkled PEDOT:PSS film-based stretchable and transparent triboelectric nanogenerator for wearable energy harvesters and active motion sensors, Adv. Funct. Mater. 28 (2018), 1803684, https://doi.org/10.1002/adfm.201803684.

[36] C. Lu, J. Chen, T. Jiang, G. Gu, W. Tang, Z.L. Wang, A stretchable, flexible triboelectric nanogenerator for self-powered real-time motion monitoring, Adv. Mater. Technol. 3 (2018), 1800021, https://doi.org/10.1002/admt.201800021.

[37] D. Choi, S. Yang, C. Lee, W. Kim, J. Kim, J. Hong, Highly surface-embossed polydimethylsiloxane-based triboelectric nanogenerators with hierarchically nanostructured conductive Ni-Cu fabrics, ACS Appl. Mater. Interfaces 10 (2018) 33221–33229, https://doi.org/10.1021/acsami.8b10613.

[38] A.F. Diaz, R.M. Felix-Navarro, A semi-quantitative triboelectric series for polymeric materials: the influence of chemical structure and properties, J. Electrost. 62 (2004) 277–290, https://doi.org/10.1016/j.elstat.2004.05.005.

[39] H.S. Wang, C.K. Jeong, M.-H. Seo, D.J. Joe, J.H. Han, J.-B. Yoon, K.J. Lee, Performance-enhanced triboelectric nanogenerator enabled by wafer-scale nanogrates of multistep pattern downscaling, Nano Energy 35 (2017) 415–423, https://doi.org/10.1016/j.nanoen.2017.04.012.

[40] F.-R. Fan, L. Lin, G. Zhu, W. Wu, R. Zhang, Z.L. Wang, Transparent triboelectric nanogenerators and self-powered pressure sensors based on micropatterned plastic films, Nano Lett. 12 (2012) 3109–3114, https://doi.org/10.1021/nl300988z.

[41] V. Nguyen, R. Zhu, R. Yang, Environmental effects on nanogenerators, Nano Energy 14 (2015) 49–61, https://doi.org/10.1016/j.nanoen.2014.11.049.

[42] E.C. Larson, T. Lee, S. Liu, M. Rosenfeld, S.N. Patel, Accurate and privacy-preserving cough sensing using a low-cost microphone, in: Proceedings of the 13th International Conference on Ubiquitous Computing, UbiComp '11, 17–21 September, 2011, Beijing, China. Association for Computing Machinery: New York. https://doi.org/10.1145/2030112.2030163.

[43] P.G. Gibson, A.B. Chang, N.J. Glasgow, P.W. Holmes, A.S. Kemp, P. Katelaris, L. I. Landau, S. Mazzone, P. Newcombe, P. Van Asperen, A.E. Vertigan, CICADA: cough in children and adults: diagnosis and assessment. Australian cough guidelines summary statement, Med. J. Aust. 192 (2010) 265–271, https://doi.org/10.5694/j.1326-5377.2010.tb03504.x.

[44] N.H.L. Leung, D.K.W. Chu, E.Y.C. Shiu, K.-H. Chan, J.J. McDevitt, B.J.P. Hau, H.-L. Yen, Y. Li, D.K. Ip, J.S.M. Peiris, W.-H. Seto, G.M. Leung, D.K. Milton, B. J. Cowling, Respiratory virus shedding in exhaled breath and efficacy of face masks, Nat. Med. 26 (2020) 676–680, https://doi.org/10.1038/s41591-020-0843-2.

[45] C.J. Duncan, S. Scott, What caused the black death? Postgrad. Med. J. 81 (2005) 315–320, https://doi.org/10.1136/pgmj.2004.024075.

[46] T. Drugman, J. Urbain, N. Bauwens, R. Chessini, A.-S. Aubriot, P. Lebecque, T. Dutoit, Audio and contact microphones for cough detection, in: Proceedings of the 13th Annual Conference of the International Speech Communication Association, 9–13 September, 2012 Portland, OR.
[47] L.-Q. Tao, K.-N. Zhang, H. Tian, Y. Liu, D.-Y. Wang, Y.-Q. Chen, Y. Yang, T.-L. Ren, Graphene-paper pressure sensor for detecting human motions, ACS Nano 11 (2017) 8790–8795, https://doi.org/10.1021/acsnano.7b02826.
[48] L.-Q. Tao, H. Tian, Y. Liu, Z.-Y. Ju, Y. Pang, Y.-Q. Chen, D.-Y. Wang, X.-G. Tian, J.-C. Yan, N.-Q. Deng, Y. Yang, T.-L. Ren, An intelligent artificial throat with sound-sensing ability based on laser-induced graphene, Nat. Commun. 8 (2017) 14579, https://doi.org/10.1038/ncomms14579.
[49] K. Roy, S.K. Ghosh, A. Sultana, S. Garain, M. Xie, C.R. Bowen, K. Henkel, D. Schmeißer, D. Mandal, A self-powered wearable pressure sensor and pyroelectric breathing sensor based on GO interfaced PVDF nanofibers, ACS Appl. Nano Mater. 2 (2019) 2013–2025, https://doi.org/10.1021/acsanm.9b00033.
[50] J. Choi, D. Kwon, K. Kim, J. Park, D. Del Orbe, J. Gu, J. Ahn, I. Cho, Y. Jeong, Y. Oh, I. Park, Synergetic effect of porous elastomer and percolation of carbon nanotube filler toward high performance capacitive pressure sensors, ACS Appl. Mater. Interfaces 12 (2020) 1698–1706, https://doi.org/10.1021/acsami.9b20097.
[51] J. Choi, D. Kwon, B. Kim, K. Kang, J. Gu, J. Jo, K. Na, J. Ahn, D. Del Orbe, K. Kim, J. Park, J. Shim, J.-Y. Lee, I. Park, Wearable self-powered pressure sensor by integration of piezo-transmittance microporous elastomer with organic solar cell, Nano Energy 74 (2020), 104749, https://doi.org/10.1016/j.nanoen.2020.104749.
[52] F. Peng, D. Liu, W. Zhao, G. Zheng, Y. Ji, K. Dai, L. Mi, D. Zhang, C. Liu, C. Shen, Facile fabrication of triboelectric nanogenerator based on low-cost thermoplastic polymeric fabrics for large-area energy harvesting and self-powered sensing, Nano Energy 65 (2019), 104068, https://doi.org/10.1016/j.nanoen.2019.104068.



Junseong Ahn is a Ph.D. candidate at the Korea Advanced Institute of Science and Technology (KAIST). He received his M.S. degree at KAIST in 2019. His current research interest is focused on micro/nano structuring, and their application to sensors/energy harvesting devices.



Zhi-Jun Zhao is a post-doctoral researcher at the Korea Institute of Machinery & Materials (KIMM). He received his Ph.D. degree at Pusan National University in 2018. His research interests are micro-nanofabrication, optical devices, nanomaterial-based sensors, and flexible & wearable electronics.



Jungrak Choi is a Ph.D. candidate at the Korea Advanced Institute of Science and Technology (KAIST). He received his M.S. degree at KAIST and DTU in 2018. His current research interest is focused on soft sensors and stretchable electronics for healthcare applications.



Yongrok Jeong is a researcher at the Korea Institute of Machinery & Materials (KIMM). He received his M.S. degree at KAIST in 2018. His current research interest is focused on micro/nano scale structuring and its usage in sensor/actuator systems.



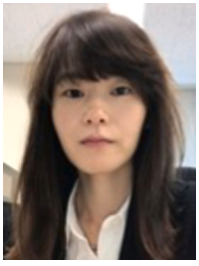
SoonHyoung Hwang is working as a senior researcher at the Korea Institute of Machinery & Materials (KIMM) in South Korea. He received his doctoral degree from the Department of Materials Science and Engineering of Seoul National University in February 2018. His present research theme involves plasmonic nano-structure fabrication by nanotransfer printing, nanoimprint lithography, E-beam lithography, and KrF lithography. He has experience in the design and fabrication of nano/micro plasmonic optical structures using metals as well as non-metallic materials such as dielectric materials.



Jiwoo Ko is a Ph.D. candidate at the Korea Advanced Institute of Science and Technology (KAIST). She received her M.S. degree at KAIST in 2018. Her current research interest is focused on nanotransfer printing onto special substrates.



Jimin Gu is a Ph.D. candidate at the Korea Advanced Institute of Science and Technology (KAIST). She received her M.S. degree at KAIST in 2019. Her current research interest is focused on soft sensors and stretchable electronics for biomedical and healthcare applications.



Sohee Jeon is a senior researcher at the Korea Institute of Machinery & Materials (KIMM). She received her Ph.D. degree at Seoul National University in 2014. Her current research interest is focused on nano/micro fabrication toward optoelectronics and biomedical applications.



Jaeho Park is a post-doctoral researcher at the Korea Advanced Institute of Science and Technology (KAIST). He received his Ph.D. degree at KAIST in 2019. His current research interest is focused on microscale biosensors and sensor-integrated systems toward biomedical applications.



Mingu Kang is an M.S. Candidate at the Korea Advanced Institute of Science and Technology (KAIST). He received his B. S. from Hanyang University in 2019. His current research interest is focused on nanofabrication and nanomaterial-based sensors.



Dionisio Del Orbe received his Bachelor's degree from Western Michigan University in 2012 and Master's degree from Rochester Institute of Technology in 2015. Currently, he is a Ph.D. student in Prof. Inkyu Park's Micro and Nano Transducer (MINT) Laboratory at the Korea Advanced Institute of Science and Technology (KAIST). His research interests include flexible physical sensors and chemical gas sensors.



Incheol Cho received his B.S. and M.S. degrees from the Department of Mechanical Engineering of the Korea Advanced Institute of Science and Technology (KAIST) in 2015 and 2017, respectively. He is currently a Ph.D. student in the Micro/Nano Transducers (MINT) research group at KAIST. His research interests are low power environmental sensors, nanoscale functional materials, and micro/nano fabrication.



Hyeok-Joong Kang is a researcher at the Korea Institute of Machinery & Materials (KIMM). He received his M.S. degree at Seoul National University in 2014. His current research interest is focused on the meta-materialistic optical characteristics of nanoscale structures and its industrial applications.



Moonjeong Bok is a post-doctoral researcher at the Korea Institute of Machinery & Materials (KIMM). She received her Ph.D. degree at Dankook University in 2020. Her current research interest is focused on nano/micro fabrication and drug delivery systems for biomedical applications.



Jun-Ho Jeong is a principal researcher at the Korea Institute of Machinery & Materials (KIMM). He is also a faculty member of the Department of Nano-Mechatronics at the University of Science and Technology (UST). He received his B.S., M.S., and Ph.D. from Hanyang University (1990), Korea Advanced Institute of Science and Technology (KAIST) (1993), and KAIST (1998), respectively, all in mechanical engineering. His research interests are nanoimprinting, nanofabrication, holograms, microneedles, and drug delivery.



Inkyu Park received his B.S., M.S., and Ph.D. from KAIST (1998), UIUC (2003), and UC Berkeley (2007), respectively, all in mechanical engineering. He has been with the Department of Mechanical Engineering at KAIST since 2009 as a faculty member and is currently a KAIST Chair Professor. His research interests include nanofabrication, smart sensors, nanomaterial-based sensors, and flexible & wearable electronics. He has published more than 85 international journal articles (SCI indexed) and 130 international conference proceedings in the area of MEMS/NANO engineering. He is a recipient of the IEEE NANO Best Paper Award (2010) and HP Open Innovation Research Award (2009–2012).